Front. Earth Sci. 2023, 17(2): 378–390
https://doi.org/10.1007/s11707-022-1023-0

RESEARCH ARTICLE

Performance of the Large Field of View Airborne Infrared Scanner and its application potential in land surface temperature retrieval

Chao WANG[1,2], Zhiyuan LI[1,2], Xiong XU (✉)[1,2,3], Xiangsui ZENG[1,2], Jia LI[1,2], Huan XIE[1,2], Yanmin JIN[1,2], Xiaohua TONG[1,2]

1 College of Surveying and Geo-informatics, Tongji University, Shanghai 200092, China
2 Shanghai Key Laboratory for Planetary Mapping and Remote Sensing for Deep Space Exploration, Tongji University, Shanghai 200092, China
3 Frontiers Science Center for Intelligent Autonomous Systems, Tongji University, Shanghai 200092, China

Abstract The Large Field of View Airborne Infrared Scanner is a newly developed multi-spectral instrument that collects images from the near-infrared to long-wave infrared channels. Its data can be used for land surface temperature (LST) retrieval and environmental monitoring. Before data application, quality assessment is an essential procedure for a new instrument. In this paper, based on the data collected by the scanner near the Yellow River in Henan Province, the geometric and radiometric qualities of the images are first evaluated. The absolute geolocation accuracy of the ten bands of the scanner is approximately 5.1 m. The ground sampling distance is found to be varied with the whisk angles of the scanner and the spatial resolution of the images. The band-to-band registration accuracy between band one and the other nine bands is approximately 0.25 m. The length and angle deformations of the ten bands are approximately 0.67% and 0.3°, respectively. The signal-to-noise ratio (SNR) and relative radiometric calibration accuracy of bands 4, 9, and 10 are relatively better than those of the other bands. Secondly, the radiative transfer equation (RTE) method is used to retrieve the LST from the data of the scanner. Measurements of *in situ* samples are collected to evaluate the retrieved LST. Neglecting the samples with unreasonable retrieved LST, the bias and RMSE between *in situ* LST measured by CE312 radiometer and retrieved LST are −0.22 K and 0.94 K, and the bias and RMSE are 0.27 K and 1.59 K for the InfReC R500-D thermal imager, respectively. Overall, the images of the Large Field of View Airborne Infrared Scanner yield a relatively satisfactory accuracy for both LST retrieval and geometric and radiometric qualities.

Received September 21, 2022; accepted October 12, 2022

E-mail: xvxiong@tongji.edu.cn

Keywords Large Field of View Airborne Infrared Scanner, quality assessment, thermal infrared remote sensing, land surface temperature retrieval

1 Introduction

Remotely sensed thermal infrared (TIR) images have been widely used to retrieve land surface temperature (LST) and land surface emissivity (LSE) (Quattrochi and Luvall, 1999; Sobrino et al., 2008; Nie et al., 2021; Renet al., 2022), detect geothermal anomalies (Coolbaugh et al., 2007), monitor volcano activities (Carter and Ramsey, 2010), explore geological ore, monitor crop growth status (Feng et al., 2022), etc. In these applications, LST is a parameter of considerable importance to retrieve, since it is a key parameter for understanding the physical processes of land surface energy and water balance on regional and global scales (Zhang et al., 2008; Karnieli et al., 2010; Eleftheriou et al., 2018). More specifically, many environmental monitoring studies, such as those on urban climate (Lemus-Canovas et al., 2020), the greenhouse effect (Parida et al., 2021) and drought monitoring (Yang et al., 2020), heavily rely on accurate LST.

A series of satellite and airborne sensors have been developed to collect TIR data and retrieve LST, such as Advanced Very High Resolution Radiometer (AVHRR) (Urban et al., 2013), Moderate Resolution Imaging Spectroradiometer (MODIS) (Duan et al., 2019), Advanced Spaceborne Thermal Emission Reflection Radiometer (ASTER) (Liu and Pu, 2008), Landsat Thematic Mapper (TM) (Weng et al., 2014), Airborne Hyperspectral Scanner (AHS) (Qian et al., 2015), Thermal Airborne Hyperspectral Imager (TASI) (Li et al., 2016), and Digital Airborne Imaging Spectrometer (DAIS) (Sobrino et al., 2004),

etc. Compared with the satellite sensors, airborne sensors have higher spatial resolution and a more flexible revisit period (potentially hours), allowing for the acquisition of more detailed LST mapping of the local area (Zhu et al., 2016). The Large Field of View Airborne Infrared Scanner is a newly developed sensor by the China High-Resolution Earth Observation Major Special Aviation Observation System Program. The scanner operates in ten bands: one near-infrared (NIR) band, three short-wave infrared (SWIR) bands, two mid-wave infrared (MWIR) bands, and four long-wave infrared (LWIR) bands. The field of view (FOV) angle is ± 50° (Ye et al., 2017). The specifications of the above mentioned airborne sensors and the Large Field of View Airborne Infrared Scanner are shown in Table 1. It can be found that the Large Field of View Airborne Infrared Scanner features a larger FOV and more detector columns. In this study, the TIR LWIR data obtained by the Large Field of View Airborne Infrared Scanner are tested to retrieve the LST of the study area.

Various approaches have been published to estimate LST from remotely sensed TIR data. These methods can be generally divided into two categories: single channel and multi-channel methods. The single-channel methods are represented by the radiative transfer equation (RTE) method (Price, 1983), Jimenez-Mufloz and Sobrino's algorithm (Jiménez-Muñoz and Sobrino, 2003), and Qin et al.'s algorithm (Qin et al., 2001). The main procedure of the RTE method is to retrieve LST by the inversion of the Planck's law based on the radiative transfer equation (Price, 1983). Jimenez-Mufloz and Sobrino's algorithm can estimate LST without *in situ* radio soundings or effective mean atmospheric temperature values and can be applied to thermal sensors characterized with a FWHM (Full-Width Half-Maximum) of approximately 1 mm. Qin et al.'s algorithm retrieves the LST with three parameters: LSE, atmospheric transmittance, and effective mean atmospheric temperature. Jimenez-Mufloz and Sobrino's and Qin et al.'s algorithms are both based on Landsat5 TM6 images. The temperature calculation equations of these two algorithms are obtained by simplifying the radiative transfer equation, and many empirical coefficients in their proposed formula are given for the characteristics of the TM6 data. The multi-channel methods include split-window methods and some other methods used more than two channels. Two TIR channels are used in split-window methods, and LST is expressed as a linear equation (Choi and Suh, 2018; Guo et al., 2020) or nonlinear equation (Coll et al., 1994; Zarei et al., 2021) of the brightness temperature of the two channels. Simulation image data or many *in situ* temperature measurements are needed to determine the parameters in the retrieval equation (Coll et al., 1994; Choi and Suh, 2018; Guo et al., 2020; Zarei et al., 2021). In addition to these methods, some specific methods have been proposed, such as the temperature and emissivity separation method (TES) (Gillespie et al., 1998), day/night method (Wan and Li, 1997; Wan, 2008), and machine learning method (Mao et al., 2011; Jia et al., 2021). These methods are generally specific to the sensors and/or time of data collection, or need many training data. Consequently, these methods lack of universality. For the data used in this study, there are no sufficient data to derive the empirical coefficients for the methods, such as Jimenez-Mufloz and Sobrino's algorithm, Qin et al.'s algorithm (single-channel algorithm), and the split-window method. Labeled data from the scanner images and its targets are also not available; thus, the machine learning method is also not applicable. Therefore, the general RTE method is more suitable for deriving the LST in this paper.

Since the Large Field of View Airborne Infrared Scanner is a newly developed instrument, a performance evaluation in both geometry and radiometry is of great importance before data application. Secondly, for future application, a capacity evaluation of LST retrieval is also needed to be conducted. To these ends, the paper is organized as follows: in Section 2, the study area and the methods of quality evaluation and LST retrieval are described. The results and discussion of the quality assessment and LST retrieval are presented in Section 3. The conclusion is drawn in Section 4.

2 Data and methods

2.1 Data description

The images and the data measured *in situ* for evaluating quality and retrieving LST were acquired on 21 October, 2020. The study area of quality evaluation is located in

Table 1 The differences between the Large Field of View Airborne Infrared Scanner and other airborne sensors

Airborne sensors	Number of channels	Spectral range/μm	FOV	Detector columns
AHS (Qian et al., 2015)	80	0.43–12.70	90°	750
TASI (Li et al., 2016)	32	8.0–11.5	40°	600
DAIS (Sobrino et al., 2004)	79	0.4–13.0	52°	512
Large Field of View Airborne Infrared Scanner	10	0.76–12.5	100°	2048/1024/512

Notes: AHS = Airborne Hyperspectral Scanner, TASI = Thermal Airborne Hyperspectral Imager, DAIS = Digital Airborne Imaging Spectrometer, FOV = field of view.

Kaifeng City, Henan Province, on the north bank of the Yellow River, centered at a latitude of 34.9°N and a longitude of 114.3°E. The main specifications of the Large Field of View Airborne Infrared Scanner are shown in Table 2. The land cover in the study area includes cropland, trees, sparse vegetation, urban areas, bare ground, and water bodies. The Ground Control Points (GCPs) used for geometric quality evaluation are measured with a Leica GNSS RTK rover. The precision of RTK measurements is better than 10 cm, which is sufficient for the quality evaluation of the scanner. Therefore, the RTK measurements are considered as ground truth. Figure 1 shows the mosaiced band nine image covering the GCPs' positions. A total of 63 GCPs are shown in Fig. 1.

To retrieve the LST and evaluate its accuracy, the *in situ* LSE and LST are measured by the Cimel CE312 high-precision IR radiometer, and the *in situ* LST is measured by the InfReC R500-D thermal imager. Because the contribution of solar radiation at the top of the atmosphere is negligible in the range of 8–14 μm, the upward solar diffusion radiance, the solar diffusion radiance reflected by the surface and the direct solar radiance reflected by the surface can be neglected without loss of accuracy (Li et al., 2013). In addition, the LSE of band ten is not available. Therefore, the experiment of LST retrieval based on band seven, band eight, and band nine is conducted first, and the band nine shows high accuracy of retrieval; thus, it is selected to estimate the LST. Figure 2 shows the position of the ten plots measured by CE312 and InfReC R500-D; the *in situ* temperature and LSE are both obtained. It should be noted that the study area of LST retrieval is not included in the study area of geometric and radiometric quality evaluation.

2.2 Quality assessment

2.2.1 Geometric quality assessment

1) Absolute geolocation accuracy

Absolute geolocation accuracy refers to the deviation between the GCPs and their corresponding coordinates in the scanner's images. According to Fig. 1, the pixels containing GCPs are relatively uniformly imaged with different whisk angles. A total of 63 GCPs are used for the evaluation of absolute geolocation accuracy, which can be expressed as

$$\Delta X_i = X_{\text{image},i} - X_{\text{GCP},i}, \tag{1}$$

$$\Delta Y_i = Y_{\text{image},i} - Y_{\text{GCP},i}, \tag{2}$$

$$D_i = \sqrt{\Delta X_i^2 + \Delta Y_i^2}, \tag{3}$$

where $X_{\text{image},i}$ and $Y_{\text{image},i}$ are the geographic coordinates of the ith GCP in the image, and $X_{\text{GCP},i}$ and $Y_{\text{GCP},i}$ are the RTK-measured coordinates of the ith GCP. The D_i is the displacement between the image-based and RTK-measured coordinates of the ith GCP. The absolute geolocation accuracy is thus obtained by averaging the D_i of all the GCPs.

2) Ground sampling distance

The ground sampling distance (GSD) describes the spacing between adjacent pixels' centers, which is a key indicator of an image's spatial resolution. In this study, it is acquired as the ratio of the RTK-measured distance (m) to the distance (expressed with number of pixel) of two GCPs on an image. According to the characteristics of the

Table 2 Specifications of the Large Field of View Airborne Infrared Scanner

Band	Channels	Spectral range/μm	Detector columns
B1	NIR	0.76–0.90	2048
B2	SWIR I	1.23–1.25	1024
B3	SWIR II	1.55–1.75	
B4		2.08–2.35	
B5	MWIR	3.50–3.90	512
B6		4.85–5.05	
B7	LWIR I	8.01–8.39	
B8		8.42–8.83	
B9	LWIR II	10.3–11.3	
B10		11.4–12.5	

Notes: NIR = near-infrared, SWIR = short-wave infrared, MWIR = mid-wave infrared, LWIR = long-wave infrared.

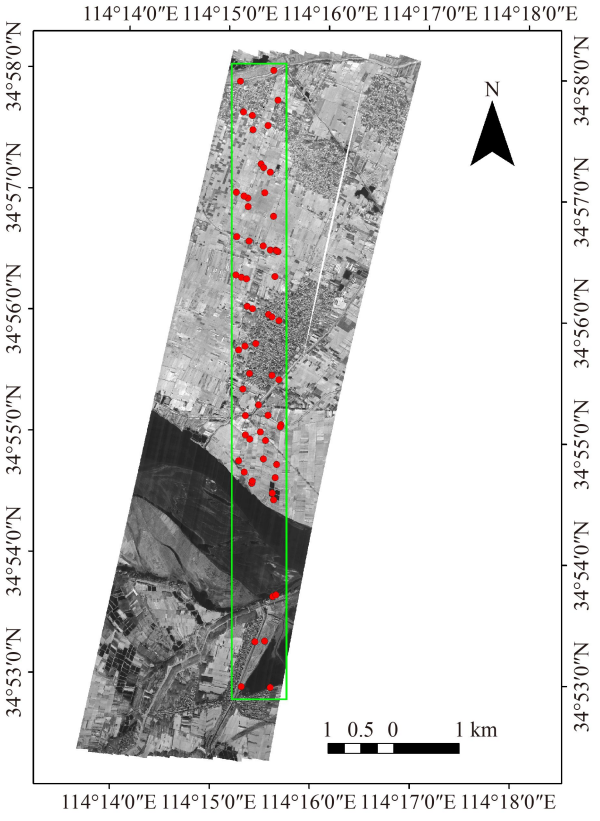

Fig. 1 Mosaic of the band nine images covering the GCPs (red points) and *in situ* measurements region (green rectangle).

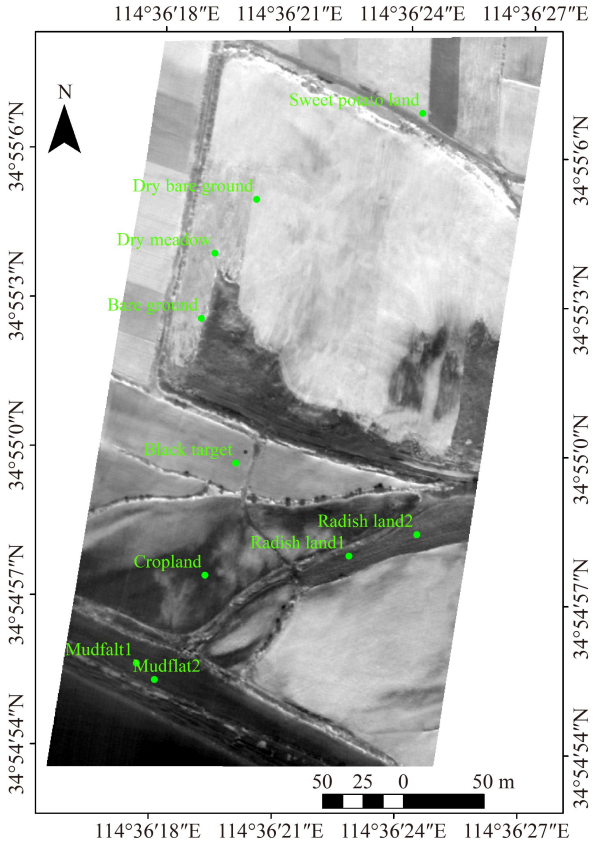

Fig. 2 Mosaic of the band nine images covering the *in situ* measurement plots (green points).

sensor's large FOV, the GSDs under various whisk angles are calculated for the evaluation of the images obtained by the newly developed scanner.

3) Band-to-band registration accuracy

Band-to-band registration (BBR) accuracy is a measure of alignment among different bands of a scene acquired by an imaging sensor. In this study, the scale-invariant feature transform (SIFT) method (Lowe, 1999) is used to extract tie points; then, the random sample consensus (RANSAC) method (Fischler and Bolles, 1981) is applied to remove the wrong-matched tie points. With the tie points, the BBR accuracy is calculated as

$$X_{\mathrm{BBR}} = \frac{1}{n}\sum_{j=1}^{n}\left|x_j^a - x_j^b\right|, \tag{4}$$

$$Y_{\mathrm{BBR}} = \frac{1}{n}\sum_{j=1}^{n}\left|y_j^a - y_j^b\right|, \tag{5}$$

$$D_{\mathrm{BBR}} = \sqrt{{X_{\mathrm{BBR}}}^2 + {Y_{\mathrm{BBR}}}^2}, \tag{6}$$

where X_{BBR} and Y_{BBR} are the BBR accuracy in X and Y directions. D_{BBR} is the overall BBR accuracy. n is the number of tie points. (x_j^a, y_j^a) and (x_j^b, y_j^b) are the geographic coordinates of the j^{th} tie point in band a and band b, respectively.

4) Geometric deformation

In this study, the length and angle deformations are calculated to evaluate the geometric deformation of the image. The length and angle deformations are expressed as

$$\Delta D = \frac{\left|D^0 - D^{\mathrm{g}}\right|}{D^{\mathrm{g}}} \times 100\%, \tag{7}$$

$$\Delta A = \left|A^0 - A^{\mathrm{g}}\right|, \tag{8}$$

where ΔD and ΔA are the length and angle deformation, respectively. D^0 is the distance of the image pixels with two GCPs. D^{g} is the distance of the ground-truth coordinates of the same GCPs. A^{g} is the angle of two lines composed by three GCPs measured by RTK. A^0 is the angle composed by the same three GCPs matched in the image.

2.2.2 Radiometric quality assessment

1) Signal-to-noise ratio

Noise is one of the major contributors to the overall instrument uncertainty. Its determination is essential for evaluating the instrument performance (Wang et al., 2018). In this study, the inverse coefficient of variation (ICV) is used to evaluate the signal-to-noise ratio (SNR), and the ICV is expressed as (Bouali and Ladjal, 2011)

$$ICV = \frac{m}{std}, \tag{9}$$

where m and std are the mean and standard deviation of DN values. The index ICV is computed in homogeneous regions.

2) Relative radiometric calibration accuracy

The process of quantifying radiometric response variation in each detector relative to each other is considered as relative radiometric calibration (Kabir et al., 2020), which can be evaluated by the generalized noise (Hu and Zhang, 2007). The generalized noise is expressed by

$$R = \frac{1}{ave}\frac{1}{n}\sum_{i=1}^{n}\left|DN(i) - ave\right|, \tag{10}$$

where ave is the average DN value of the whole image. n is the number of columns of the image. $DN(i)$ is the average DN value of the i^{th} column. The larger the value of R is, the worse the quality of the relative radiometric calibration. The generalized noise is calculated in the same homogeneous regions as ICV.

2.3 LST retrieval method

In this paper, the RTE method (Price, 1983) is used to

retrieve LST from the images of the Large Field of View Airborne Infrared Scanner. In the TIR wavelength, the radiative transfer equation is expressed as

$$L_{\text{sensor},\lambda} = \left[\varepsilon_\lambda B_\lambda(T_S) + (1-\varepsilon_\lambda) L^{\downarrow}_{\text{atm},\lambda}\right] \cdot \tau_\lambda + L^{\uparrow}_{\text{atm},\lambda}, \quad (11)$$

where L_{sensor} is the radiance measured by the sensor. ε is the LSE. τ is the total atmospheric transmissivity. $L^{\downarrow}_{\text{atm}}$ and $L^{\uparrow}_{\text{atm}}$ are the down-welling and up-welling atmospheric radiance, respectively. $B(T_S)$ is the blackbody radiance given by Planck's law, and T_S is the LST. Planck's law can be given by the following expression:

$$B_\lambda(T_S) = \frac{c_1 \lambda^{-5}}{\exp\left(\frac{c_2}{\lambda T_S}\right) - 1}, \quad (12)$$

with $c_1 = 1.19104 \times 10^8\ \text{W} \cdot \mu\text{m}^4 \cdot \text{m}^{-2} \cdot \text{sr}^{-1}$, and $c_2 = 1.43877 \times 10^4\ \mu\text{m} \cdot \text{K}$. Combining Eqs. (11) and (12), the LST can be calculated as

$$T_S = \frac{c_2 \lambda^{-1}}{\ln\left[\left(\frac{\varepsilon_\lambda \tau_\lambda c_1 \lambda^{-5}}{L_{\text{sensor},\lambda} - L^{\uparrow}_{\text{atm},\lambda} - (1-\varepsilon_\lambda) L^{\downarrow}_{\text{atm},\lambda} \tau_\lambda}\right) + 1\right]}. \quad (13)$$

In Eq. (13), the total atmospheric transmissivity, down-welling atmospheric radiance, and up-welling atmospheric radiance can be predicted by the MODTRAN (MODerate resolution atmospheric TRANsmission) (Anderson et al., 2000) radiative transfer code with the real-time atmospheric profiles of the study area.

3 Results and discussion

3.1 Geometric quality assessment

In this section, the evaluation results of absolute geolocation accuracy, ground sampling distance, band-to-band registration accuracy, and the geometric deformation of the images obtained by the Large Field of View Airborne Infrared Scanner are presented. To determine the absolute geolocation accuracy, a set of 63 GCPs is used and their coordinates have been compared with the corresponding positions in the image. Table 3 shows the averaged ΔX and ΔY, and the absolute geolocation accuracy of all the GCPs in the ten bands.

As seen from Table 3, the average displacement of the 63 GCPs in the X and Y directions are quite stable for the ten bands, which are approximately 3.0 m and 3.5 m, respectively. Additionally, the absolute geolocation accuracy is approximately 5.1 m. The results show that the geolocation accuracy is band-independent. The relationship between the absolute geolocation accuracy and the whisk angle of pixels containing the GCPs is shown in Fig. 3. When the whisk angle is smaller than 25°, the variation in the absolute geolocation accuracy is relatively small, with a maximum, minimum, and average value of 6.63 m, 0.85 m, and 3.73 m, respectively. However, when the whisk angle is larger than 25°, the absolute geolocation accuracy of some GCPs starts to deteriorate, reaching a high value of 17.67 m in this study. There are 23 GCPs that have a whisk angle larger than 25°, and nine of them have errors higher than 8 m, suggesting that the geolocation accuracy may be correlated with the whisk angle.

In this study, each GCP is paired, and these pairs are then used to evaluate the GSD of the Large Field of View Airborne Infrared Scanner. Table 4 shows the GSD under different whisk angles and the average GSD. It should be noted that for the GSD under different whisk angles, only the pairs for which the GCPs had a whisk angle within ± 2.5° of the angle in Table 4 are taken into consideration, and the average in Table 4 represents the average GSD of all the GCP pairs. Figure 4 shows the relationship

Table 3 The average displacement in the X and Y directions, and the absolute geolocation accuracy in the ten bands

Band	$\triangle X$/m	$\triangle Y$/m	Absolute geolocation accuracy/m
B1	2.873	3.531	5.013
B2	2.955	3.597	5.119
B3	2.899	3.513	5.017
B4	2.995	3.485	5.065
B5	2.918	3.498	5.013
B6	3.014	3.447	5.030
B7	3.038	3.453	5.052
B8	3.073	3.521	5.123
B9	3.030	3.448	5.030
B10	3.143	3.458	5.116

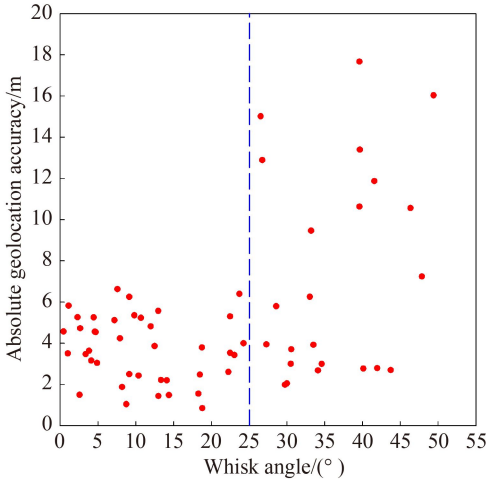

Fig. 3 Comparison of the whisk angle of the image pixels containing the 63 GCPs and the averaged absolute geolocation accuracy in ten bands for each GCP.

Table 4 The average ground sampling distance (m/pixel) under different whisk angles and the average ground sampling distance (m/pixel) of all GCP pairs

Band	5°	10°	20°	30°	40°	50°	Average
B1	0.116	0.122	0.125	0.142	0.171	0.225	0.137
B2	0.234	0.245	0.250	0.282	0.341	0.450	0.274
B3	0.233	0.245	0.249	0.282	0.339	0.447	0.274
B4	0.234	0.245	0.249	0.284	0.339	0.447	0.274
B5	0.437	0.456	0.486	0.554	0.640	0.854	0.514
B6	0.437	0.457	0.489	0.556	0.644	0.854	0.514
B7	0.437	0.456	0.482	0.552	0.643	0.855	0.514
B8	0.437	0.457	0.483	0.554	0.650	0.856	0.514
B9	0.437	0.457	0.484	0.554	0.642	0.853	0.514
B10	0.438	0.457	0.484	0.551	0.641	0.855	0.514

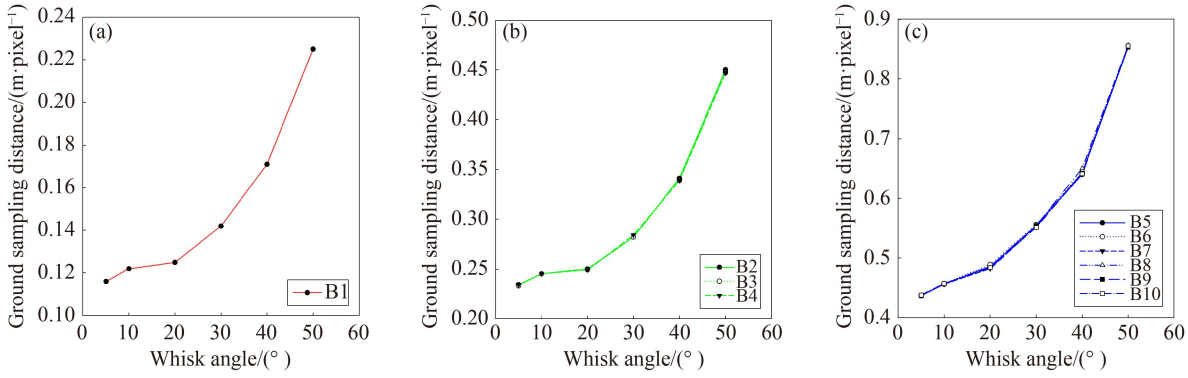

Fig. 4 The relationship between the whisk angle and ground sampling distance of (a) B1, (b) B2, B3, and B4, and (c) B5, B6, B7, B8, B9, and B10.

between the whisk angle and ground sampling distance of different bands. From Table 4 and Fig. 4, it can be seen that: 1) the average GSD of B1 is 0.137 m/pixel, the average GSDs of B2, B3, and B4 are 0.274 m/pixel, and the average GSDs of the other six bands are 0.514 m/pixel; 2) the GSD at the whisk angle of 50° is approximately twice as high as that at 5°; 3) the GSD increases with the increase in imaging whisk angle; and 4) for bands with the same nominal spatial resolution, the GSDs under different whisk angles are generally consistent, i.e., band-independent.

As mentioned in Section 2, the band-to-band registration accuracy is also used to evaluate the geometric quality. With band one set as the reference, the BBR accuracy between band one and the other nine bands can thus be calculated. The resulting BBRs are shown in Table 5. The BBR in the X and Y directions is approximately 0.18 m and 0.16 m, respectively, with a maximum of 0.26 m. The overall BBR accuracy of each band is approximately 0.25 m, and the maximum value is the BBR accuracy between band one and band two—0.314 m in this study. Meanwhile, to compare the BBR accuracy under different whisk angles, the BBR accuracy between band one and band two in the X and Y directions of different lines is shown in Fig. 5. The BBR accuracy in different image lines is relatively stable, i.e., the BBR accuracy is independent of the whisk angle. In addition, the number of tie points decreases with the increase of the error of band-to-band registration in both X and Y directions (e.g., Figs. 5(c) and 5(d)), thus, no systematic error is noted

Table 5 The overall band-to-band registration accuracy and the band-to-band registration accuracy in the X and Y directions between band one and different bands

Band	X_{BBR}/m	Y_{BBR}/m	Band-to-band registration accuracy/m
B2	0.177	0.259	0.314
B3	0.146	0.138	0.201
B4	0.182	0.142	0.231
B5	0.241	0.151	0.285
B6	0.167	0.146	0.222
B7	0.150	0.180	0.234
B8	0.258	0.164	0.306
B9	0.177	0.156	0.236
B10	0.190	0.167	0.253

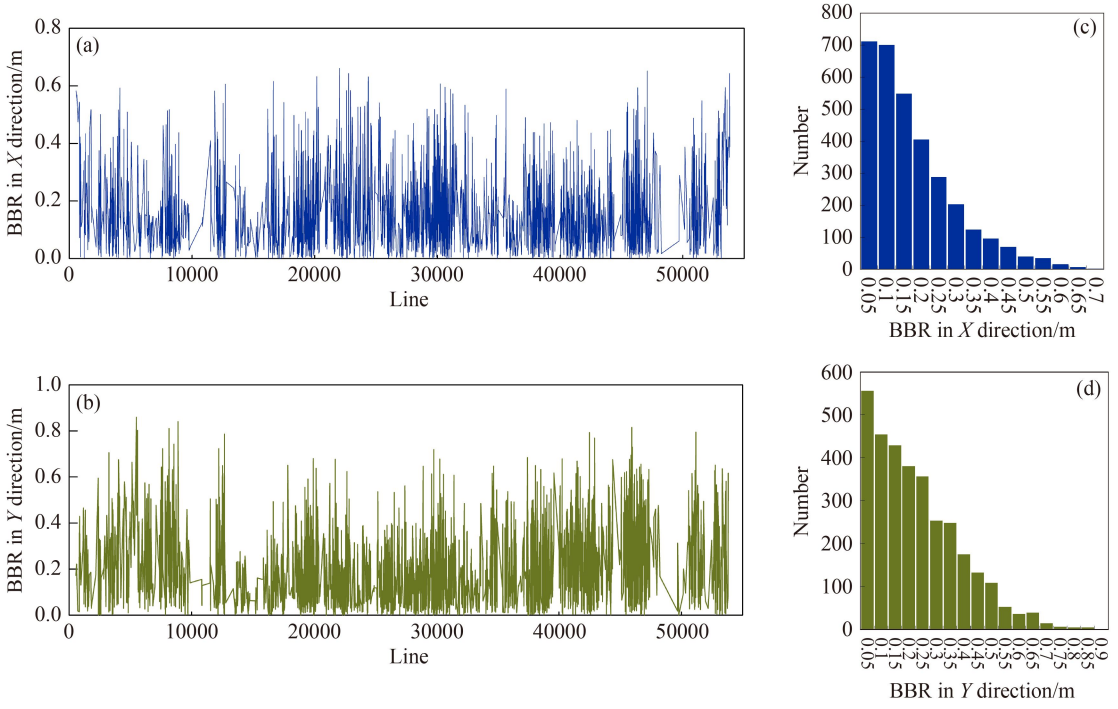

Fig. 5 The band-to-band registration accuracy between band one and band two of different lines in the (a) *X* and (b) *Y* directions. (c) and (d) are the corresponding histogram of band-to-band registration accuracy in the *X* and *Y* directions.

between the registration of different bands.

Finally, the geometric deformation has been evaluated in terms of length and angle. The results in different bands are shown in Table 6. The length deformation of each band is the average value of the length deformation of lines constructed by every two GCPs in the same scene. Additionally, the angle deformation is the average angle constructed by every three GCPs. From Table 6, the average length deformation and angle deformation of the ten bands are approximately 0.67% and 0.3°, respectively. The number of different lengths and angles used in the evaluation are shown in Fig. 6. The distance between two GCPs varies from close to 0 km to more than 3 km, and the angle varies from 0° to 180°. Thus, the evaluation of length and angle deformation is relatively comprehensive. In Fig. 6(b), it can be seen that there are more angle measurements closing to 0° and 180°. This is due to the long and narrow shape of the image, when the GCP at the angular point is in the middle line of the other two GCPs. The angle is frequently close to 180°; otherwise, the angle is close to 0°.

Table 6 The results of length deformation and angle deformation of the ten bands

Band	Length deformation	Angle deformation
B1	0.638%	0.337°
B2	0.661%	0.315°
B3	0.653%	0.321°
B4	0.662%	0.302°
B5	0.674%	0.241°
B6	0.672%	0.304°
B7	0.684%	0.309°
B8	0.693%	0.315°
B9	0.683%	0.317°
B10	0.697%	0.298°

As mentioned above, the geometric quality of the data of the Large Field of View Airborne Infrared Scanner was evaluated from four aspects. Regarding the evaluation results, the uncertainty may arise in the following processes. First, the GCPs are matched between the scanner's images and *in situ* measurements through visual inspection. Thus, artifacts may exist. Second, though the RANSAC method is used to remove the wrong-matched tie points, the wrong-matched tie points may still exist and are used in the evaluation of BBR accuracy. Last, some uncertainty could arise from the *in situ* measurements, i.e., the coordinates of GCPs measured by RTK. The Large Field of View Airborne Infrared Scanner is a whisk broom scanner (Ye et al., 2017). As shown in Table 1, the FOV of the Large Field of View Airborne Infrared Scanner is significantly greater than that of some other commonly used airborne sensors. Therefore, the relationship between the whisk angle and geometric quality are analyzed. According to the evaluation results of geometric quality assessment, the absolute geolocation accuracy and GSD are correlated with the whisk angle. When the imaging whisk angle increases, the distance between the object and the sensor increases; thus, the GSD also increases. A bigger GSD will lead to greater

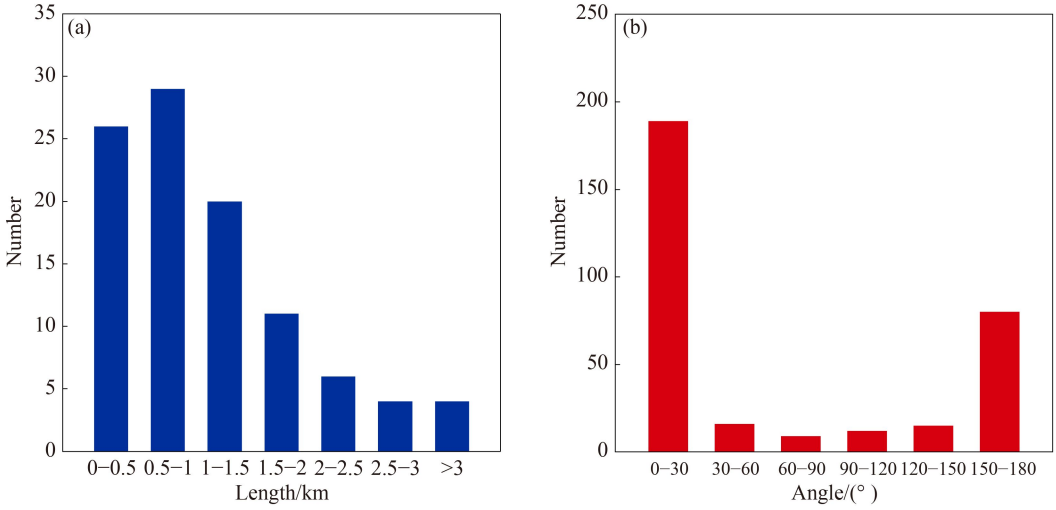

Fig. 6 Number of different (a) lengths and (b) angles used in the evaluation of geometric deformation.

error in the process of manual recognition. Additionally, this may be a possible reason for the deterioration in the absolute geolocation accuracy when the whisk angle is larger than 25°. The absolute geolocation accuracy and BBR accuracy of the Large Field of View Airborne Infrared Scanner have been compared to the accuracy of some other airborne sensors, finding that the accuracy is similar.

3.2 Radiometric quality assessment

In this study, the signal-to-noise ratio and relative radiometric calibration accuracy are used to assess the radiometric quality of the image obtained by the Large Field of View Airborne Infrared Scanner. The ICV and generalized noise are selected to represent the two evaluation indexes, respectively. The ICV and generalized noise are computed in four homogeneous regions within a window of the same size and plot. The four regions correspond to four land cover classes, i.e., bare ground, built-up area, vegetation field, and water body. The region of built-up area of every band is shown in Fig. 7. Tables 7 and 8 show the statistics of the generated ICV and generalized noise.

From Table 7, and Figs. 7 and 8, it can be seen that the performance of SNR varies across the ten bands. The ICV of B1, B3, and B5 is relatively smaller than for other bands, and there is obvious streak noise in the B3. The ICV of B4, B9, and B10 is larger than 500; thus, the noise level of the three bands is relatively low. More targets' information could be obtained from these three bands. The relative radiometric calibration accuracy of all ten bands is below 0.5%, which yields a relatively good radiometric calibration. In addition, the generalized noise of B1, B3, and B5 is more than 0.1%, and the effect of the relative radiometric calibration of the three bands is

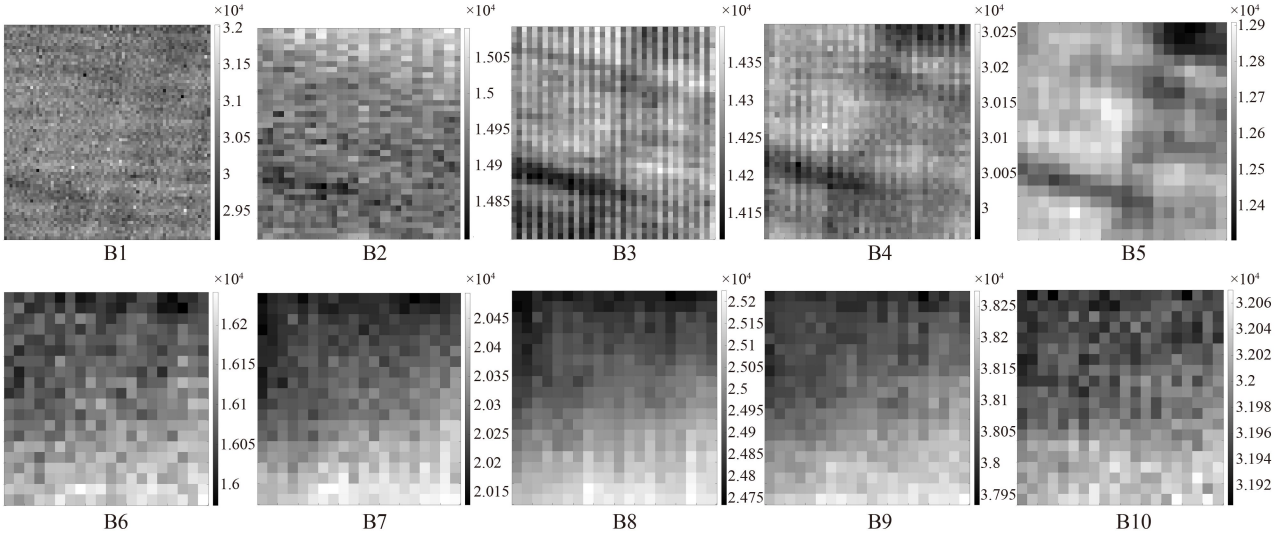

Fig. 7 Images of the DN value for the sample of built-up area of the ten bands.

Table 7 The average signal-to-noise ratio and relative radiometric calibration accuracy of the ten bands

Band	Signal-to-noise ratio	Relative radiometric calibration accuracy
B1	92.520	0.230%
B2	434.816	0.054%
B3	222.512	0.234%
B4	634.234	0.065%
B5	161.266	0.244%
B6	406.591	0.067%
B7	446.288	0.072%
B8	424.414	0.083%
B9	1057.488	0.027%
B10	1442.267	0.016%

Table 8 The average signal-to-noise ratio and relative radiometric calibration accuracy of the four regions

Land cover	Signal-to-noise ratio	Relative radiometric calibration accuracy
Bare ground	467.189	0.110%
Built-up area	372.749	0.115%
Vegetation field	452.198	0.113%
Water body	836.821	0.099%

relatively poor compared with other bands. From Table 8 and Fig. 8, for the four land cover classes, it can be seen that the SNR of the water body is relatively higher than that of the other three regions, and the relative radiometric calibration accuracy of the four regions is basically consistent.

3.3 The retrieval of LST

In Section 2, we described the principle of the RTE LST retrieval method. To verify the feasibility of this method for the data obtained by the Large Field of View Airborne Infrared Scanner, a validation experiment is conducted based on the *in situ* LST and LSE measured by CE312 IR and the InfReC R500-D. Figure 9 shows the results of *in situ* LST measured by InfReC R500-D. For each measured plot, a window of 5 × 5 pixels is cropped from the image. Within the window, the average at-sensor radiance of the pixels is calculated as L_{sensor}. The atmospheric profiles data are obtained from the European Centre for Medium-Range Weather Forecasts (ECWMF) reanalysis v5 (ERA5) (Hoffmann et al., 2019). The temporal resolution and spatial resolution of the reanalysis data are 3 h and 0.75° × 0.75°, respectively. Through LST retrieval tests, it is found that the atmospheric humidity has a larger impact on the retrieval accuracy than other meteorological factors. In general, the impact of ECWMF forecast errors of atmospheric humidity on LST retrievals is less than 0.5 K (Freitas et al., 2010). With the aid of MODTRAN, the atmospheric transmittance, atmospheric downwelling radiance, and upwelling radiance in a given channel could be derived. Then, the LST of each plot is calculated based on Eq. (13).

Tables 9 and 10 show the results of the *in situ* measurement of LST by CE312 and InfReC R500-D and the RTE-retrieved LST, and the difference between them. Figure 10 shows the correlation between the retrieved LST and the LST measured *in situ*, which overall shows a good agreement. As can be seen in Table 11, the bias, mean absolute error (MAE), standard deviation, and root mean square error (RMSE) between the LST measured *in situ* by CE312 and the retrieved LST are 0.35 K, 2.10 K, 3.12 K, and 2.98 K, respectively, for all the samples. Meanwhile, the bias, MAE, standard deviation, and RMSE of InfReC R500-D are 1.43 K, 2.21 K, 2.89 K, and 3.09 K, respectively. The error for the dry bare ground between LST measured *in situ* by CE312 and InfReC R500-D and the retrieved LST shows large variation. The main reason may be the measurement error

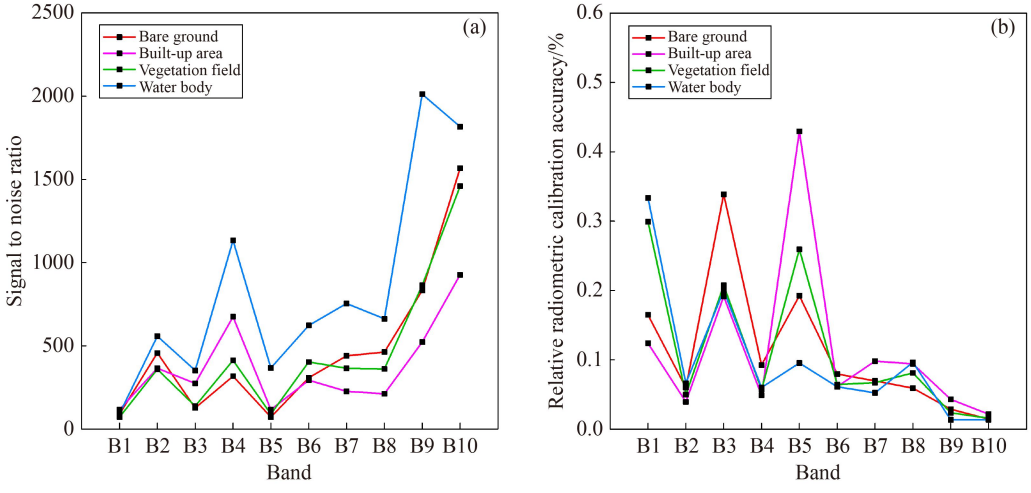

Fig. 8 (a) Signal-to-noise ratio and (b) relative radiometric calibration accuracy of the ten band in the four regions.

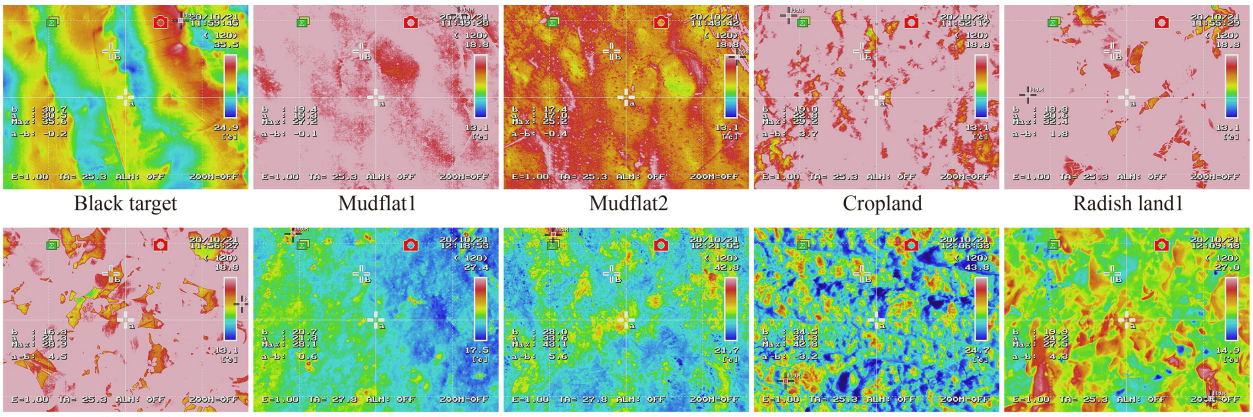

Fig. 9 The *in situ* LST of the ten plots measured by the InfReC R500-D.

Table 9 Comparison between the LST measured *in situ* by CE312 and retrieved with the RTE method

Plot	Mueasurement time (2020-10-21)	LSE (10.6 μm)	*In situ* LST/K	Retrieved LST/K	Difference/K
Black target	11:31:57	0.930	304.28	302.63	−1.65
Mudflat1	11:48:27	0.949	294.07	295.51	1.43
Mudflat2	11:51:53	0.987	292.22	292.48	0.26
Cropland	11:56:29	0.957	294.04	294.25	0.21
Radish land1	12:01:54	0.985	294.69	293.69	−1.01
Radish land2	12:06:06	0.978	295.17	294.93	−0.24
Bare ground	12:14:47	0.961	296.27	301.47	5.20
Dry meadow	12:19:39	0.962	306.17	305.65	−0.52
Dry bare ground	12:24:14	0.954	310.01	304.65	−5.35
Sweet potato land	12:49:12	0.978	297.29	302.46	5.17

Note: LSE = land surface emissivity, LST = land surface temperature.

Table 10 Comparison between the LST measured *in situ* by InfReC R500-D and retrieved with the RTE method

Plsot	Measurement time (2020-10-21)	*In situ* LST/K	Retrieved LST/K	Difference/K
Black target	11:59:45	303.65	302.63	−1.02
Mudflat1	11:49:28	292.45	295.51	3.06
Mudflat2	11:48:42	290.15	292.48	2.33
Cropland	11:52:17	295.95	294.25	−1.70
Radish land1	11:55:29	293.75	293.69	−0.06
Radish land2	11:56:27	294.45	294.93	0.48
Bare ground	12:18:53	294.45	301.47	7.02
Dry meadow	12:21:05	306.75	305.65	−1.10
Dry bare ground	12:06:33	304.45	304.65	0.20
Sweet potato land	12:09:48	297.35	302.46	5.11

Note: LST = land surface temperature.

of CE312. However, the error of bare ground and sweet potato land between the two *in situ* measured and retrieved LST are more than 5 K. Several possible reasons could account for this large discrepancy. First, for the two samples of bare ground, the error could be caused by the soil's structure, which is porous, permeable, and has variable water content, and as a result, causes the LSE measurement to be inaccurate (Herb et al., 2008). In contrast, the vegetation has higher emissivity and lower deviation than the soil (Yamamoto and Ishikawa, 2018). Secondly, according to the radiative transfer equation and Eq. (13), the inaccurate LSE (i.e., ε) will finally lead to the error in the retrieved LST. The radiance emitted directly by the surface and the down-welling atmospheric radiance are affected conversely by the LSE. The down-welling atmospheric radiance is usually much smaller than the radiance emitted directly by the surface. Thus, when the LSE is measured to be larger than the true LSE, the retrieved LST will be smaller than the true value. In a hot and humid atmosphere, a 1% error in LSE will cause a 0.3 K error in the retrieval of the LST, compared with a retrieval error even up to 0.7 K in a dry and cold atmosphere (Dash et al., 2002). Under the atmospheric conditions of this study, if the measured LSE is 0.01 more than the true LSE, the retrieved LST will be reduced by approximately 0.7 K. Thirdly, the reflectance of the infrared channel is higher in arid and semi-arid areas, which will have a bigger effect on the correction of solar radiation, and thus lead to a reduction in the retrieval accuracy (Li et al., 2013). Fourthly, the time interval

between *in situ* measurements and the image acquisition time could be another possible reason. The image acquisition time is 12:14 on October 21, 2020. According to Table 9, the time interval of the last sample (Table 9) is more than half an hour. Considering that the LST varies more at noon, the retrieved LST could have a large difference with the LST measured *in situ*. This effect could also account for the relatively large discrepancy between the LST of the first two samples in Table 9 and the two mudflat samples in Table 10.

To verify the reliability of the radiance data (i.e., the radiance transformed from the raw data of the Large Field of View Airborne Infrared Scanner) used for LST retrieval, the simulated radiance is compared with the radiance extracted from the images. The radiance can be simulated by Eqs. (11) and (12) if the atmospheric parameters (i.e., total atmospheric transmissivity, downwelling atmospheric radiance, and up-welling atmospheric radiance), LSE, and LST are known. The atmospheric parameters are derived from the MODTRAN. Additionally, the simulated radiance is then calculated based on the LST and LSE measured *in situ* by CE312. The average difference between simulated radiance and image radiance for the ten plots is approximately 10%, which is relatively large. The difference in bare ground and sweet potato land is more than 20%, which may be the main reason for the large error of the two plots. Therefore, the radiance data used in this study seem to be affected by a calibration problem. As can be seen from Table 11, if we neglect the unreasonable retrieval of bare ground, dry bare ground, and sweet potato land, the bias, MAE, standard deviation, and RMSE between LST measured *in situ* by CE312 and the retrieved LST are −0.22 K, 0.76 K, 0.99 K, and 0.94 K, respectively. Additionally, for the InfReC R500-D, the bias, MAE, standard deviation, and RMSE are 0.27 K, 1.24 K, 1.67 K, and 1.59 K, respectively, if we neglect the bare ground and sweet potato land. The LST retrieval of the Large Field of View Airborne Infrared Scanner is quite promising for future data applications.

4 Conclusions

In this study, the geometric and radiometric quality assessment and LST retrieval of the images of the newly developed Large Field of View Airborne Infrared Scanner are conducted based on the data collected near the Yellow River in Henan Province. The geometric quality is evaluated in terms of four aspects: absolute geolocation accuracy, GSD, BBR accuracy, and geometric deformation. The absolute geolocation accuracy of the ten bands is approximately 5.1 m. The accuracy starts to deteriorate when the whisk angle exceeds 25°. The GSD increases with the increase in the whisk angle, and the average GSD of the three kinds of spatial resolution images are 0.137 m/pixel, 0.274 m/pixel, and 0.514 m/pixel, respectively. The BBR accuracy between band one and the other nine bands is approximately 0.25 m. Additionally, there is no obvious correlation between the whisk angle and the BBR accuracy. The length and angle deformations of the ten bands are approximately 0.67% and 0.3°, respectively. The SNR and relative radiometric calibration accuracy of the four land cover classes are computed to evaluate the radiometric quality; most bands perform well, but the SNR and relative radiometric calibration accuracy of bands 1, 3, and 5 are comparatively worse than those of other bands. Compared with bare ground, built-up areas, and vegetation fields, water bodies have a better performance in terms of the radiometric quality.

Measurements of ten *in situ* samples are collected to evaluate the LST retrieval of the scanner. Three samples, i.e., bare ground, dry bare ground, and sweet potato land,

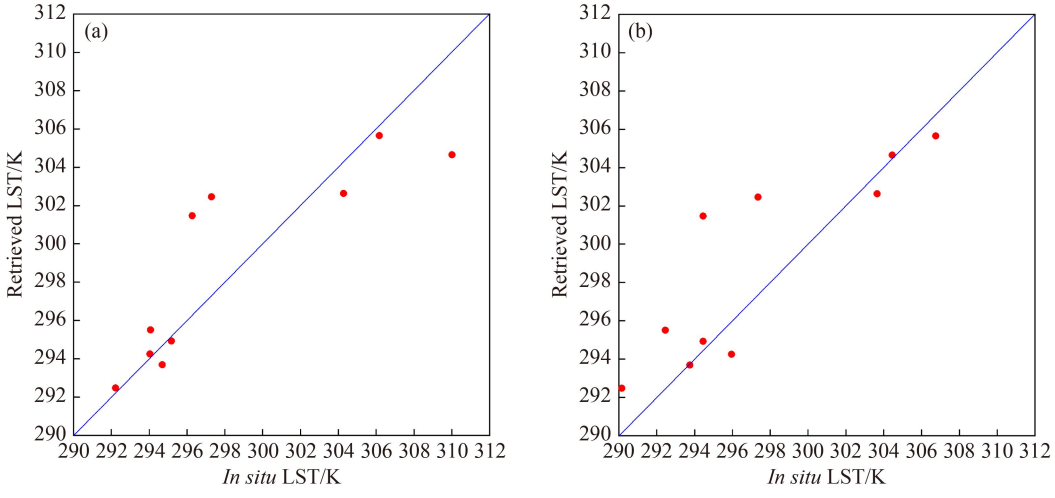

Fig. 10 Correlation between the *in situ* LST measured by (a) CE312 and (b) InfReC R500-D and the LST obtained from the RTE method.

Table 11 The statistics of the comparison between the LST measured *in situ* and the RTE-retrieved LST

Indicators	CE312		InfReC R500-D	
	all[a)]	part[b)]	all[c)]	part[d)]
Bias/K	0.35	−0.22	1.43	0.27
MAE/K	2.10	0.76	2.21	1.24
Standard deviation/K	3.12	0.99	2.89	1.67
RMSE/K	2.98	0.94	3.09	1.59

Notes: MAE = mean absolute error, RMSE = root mean square error, a) the statistics of all plots measured by CE312, b) the statistics of plots measured by CE312 without bare ground, dry bare ground, and sweet potato land, c) the statistics of all plots measured by InfReC R500-D, d) the statistics of plots measured by InfReC R500-D without bare ground and sweet potato land.

show an unreasonable retrieved LST discrepancy (> 5 K) with the *in situ* measurements. Neglecting these samples, the bias, MAE, standard deviation, and RMSE between the *in situ* LST measured by CE312 and the retrieved LST from band nine of the Large Field of View Airborne Infrared Scanner are −0.22 K, 0.76 K, 0.99 K, and 0.94 K, respectively. Additionally, when comparing the retrieved LST with the LST measured *in situ* by InfReC R500-D, the bias, MAE, standard deviation, and RMSE are 0.27 K, 1.24 K, 1.67 K, and 1.59 K, respectively, without the measurements of the bare ground and sweet potato land. This indicates a quite good retrieval accuracy compared with similar satellite infrared sensors.

In conclusion, a relatively comprehensive quality assessment for the new instrument, Large Field of View Airborne Infrared Scanner, is conducted in this paper. The scanner shows a relatively stable accuracy of geometric quality in different bands, and the radiometric quality is proved to be acceptable. In addition, the applicability of the RTE method for the LST retrieval of band nine of the scanner is validated, thus, the scanner could be used to obtain high-resolution LST maps. And the evaluation results could be used as reference for the further applications of the scanner. Additionally, the accuracy of LST retrieval could be further verified with more observations.

Acknowledgments This work was supported by the National Natural Science Foundation of China (Grant Nos. 42171363, 41804166, and 41971299), High-Resolution Earth Observation Major Special Aviation Observation System (No. 30-H30C01-9004-19/21), the Shanghai Municipal Science and Technology Major Project (No. 2021SHZDZX0100); and the Shanghai Municipal Commission of Science and Technology Project (No. 19511132101). The authors would like to thank the Aerospace Information Research Institute, Chinese Academy of Sciences, for providing the images acquired by the Large Field of View Airborne Infrared Scanner; Peking University for providing part of the *in situ* measurement; and ECMWF for providing the ERA5 data.

References

Anderson G P, Berk A, Acharya P K, Matthew M W, Bernstein L S, Chetwynd J H, Dothe H, Adler-Golden S M, Ratkowski A J, Felde G W, Gardner J A, Hoke M L, Richtsmeier S C, Pukall B, Mello J B, Jeong L S (2000). MODTRAN4: radiative transfer modeling for remote sensing. In: Algorithms for Multispectral, Hyperspectral, and Ultraspectral Imagery VI. Washington: SPIE: 176–183

Bouali M, Ladjal S (2011). Toward optimal destriping of MODIS data using a unidirectional variational model. IEEE Trans Geosci Remote Sens, 49(8): 2924–2935

Carter A, Ramsey M (2010). Long-term volcanic activity at shiveluch volcano: nine years of ASTER spaceborne thermal infrared observations. Remote Sens (Basel), 2(11): 2571–2583

Choi Y Y, Suh M S (2018). Development of Himawari-8/Advanced Himawari Imager (AHI) land surface temperature retrieval algorithm. Remote Sens (Basel), 10(12): 2013

Coll C, Caselles V, Sobrino J A, Valor E (1994). On the atmospheric dependence of the split-window equation for land-surface temperature. Int J Remote Sens, 15(1): 105–122

Coolbaugh M, Kratt C, Fallacaro A, Calvin W, Taranik J (2007). Detection of geothermal anomalies using Advanced Spaceborne Thermal Emission and Reflection Radiometer (ASTER) thermal infrared images at Bradys Hot Springs, Nevada, USA. Remote Sens Environ, 106(3): 350–359

Dash P, Göttsche F M, Olesen F S, Fischer H (2002). Land surface temperature and emissivity estimation from passive sensor data: theory and practice-current trends. Int J Remote Sens, 23(13): 2563–2594

Duan S B, Li Z L, Li H, Göttsche F M, Wu H, Zhao W, Leng P, Zhang X, Coll C (2019). Validation of Collection 6 MODIS land surface temperature product using *in situ* measurements. Remote Sens Environ, 225: 16–29

Eleftheriou D, Kiachidis K, Kalmintzis G, Kalea A, Bantasis C, Koumadoraki P, Spathara M E, Tsolaki A, Tzampazidou M I, Gemitzi A (2018). Determination of annual and seasonal daytime and nighttime trends of MODIS LST over Greece - climate change implications. Sci Total Environ, 616-617: 937–947

Feng Z, Song L, Duan J, He L, Zhang Y, Wei Y, Feng W (2022). Monitoring Wheat Powdery Mildew Based on Hyperspectral, Thermal Infrared, and RGB Image Data Fusion. Sensors (Basel), 22(1): 31

Fischler M A, Bolles R C (1981). Random sample consensus: a paradigm for model fitting with applications to image analysis and automated cartography. Commun ACM, 24(6): 381–395

Freitas S C, Trigo I F, Bioucas-Dias J M, Gottsche F M (2010). Quantifying the uncertainty of land surface temperature retrievals From SEVIRI/Meteosat. IEEE Trans Geosci Remote Sens, 48(1): 523–534

Gillespie A, Rokugawa S, Matsunaga T, Cothern J S, Hook S, Kahle A B (1998). A temperature and emissivity separation algorithm for Advanced Spaceborne Thermal Emission and Reflection Radiometer (ASTER) images. IEEE Trans Geosci Remote Sens, 36(4): 1113–1126

Guo J, Ren H, Zheng Y, Lu S, Dong J (2020). Evaluation of land surface temperature retrieval from Landsat 8/TIRS images before and after stray light correction using the SURFRAD dataset. Remote Sens (Basel), 12(6): 1023

Herb W R, Janke B, Mohseni O, Stefan H G (2008). Ground surface temperature simulation for different land covers. J Hydrol (Amst), 356(3–4): 327–343

Hoffmann L, Günther G, Li D, Stein O, Wu X, Griessbach S, Heng Y, Konopka P, Müller R, Vogel B, Wright J S (2019). From ERA-Interim to ERA5: the considerable impact of ECMWF's next-generation reanalysis on Lagrangian transport simulations. Atmos Chem Phys, 19(5): 3097–3124

Hu Y, Zhang Y (2007). Analysis of relative radiometric calibration accuracy of space camera. Spacecraft Recovery & Remote Sensing, 28(4): 54–57 (in Chinese)

Jia H, Yang D, Deng W, Wei Q, Jiang W (2021). Predicting land surface temperature with geographically weighed regression and deep learning. Wiley Interdiscip Rev Data Min Knowl Discov, 11(1)

Jiménez-Muñoz J C, Sobrino J A (2003). A generalized single-channel method for retrieving land surface temperature from remote sensing data. J Geophys Res, 108(D22): 2003JD003480

Kabir S, Leigh L, Helder D (2020). Vicarious methodologies to assess and improve the quality of the optical remote sensing images: a critical review. Remote Sens (Basel), 12(24): 4029

Karnieli A, Agam N, Pinker R T, Anderson M, Imhoff M L, Gutman G G, Panov N, Goldberg A (2010). Use of NDVI and land surface temperature for drought assessment: merits and limitations. J Clim, 23(3): 618–633

Lemus-Canovas M, Martin-Vide J, Moreno-Garcia M C, Lopez-Bustins J A (2020). Estimating Barcelona's metropolitan daytime hot and cold poles using Landsat-8 land surface temperature. Sci Total Environ, 699: 134307

Li C, Tian S, Li S, Yin M (2016). Temperature and emissivity separation via sparse representation with thermal airborne hyperspectral imager data. J Appl Remote Sens, 10(4): 042003

Li Z, Tang B, Wu H, Ren H, Yan G, Wan Z, Trigo I F, Sobrino J A (2013). Satellite-derived land surface temperature: current status and perspectives. Remote Sens Environ, 131: 14–37

Liu D, Pu R (2008). Downscaling thermal infrared radiance for subpixel land surface temperature retrieval. Sensors (Basel), 8(4): 2695–2706

Lowe D G (1999). Object recognition from local scale-invariant features. In: Proceedings of the Seventh IEEE International Conference on Computer Vision. Kerkyra: IEEE: 1150–1157

Mao K, Li S, Wang D, Zhang L, Wang X, Tang H, Li Z (2011). Retrieval of land surface temperature and emissivity from ASTER1B data using a dynamic learning neural network. Int J Remote Sens, 32(19): 5413–5423

Nie J, Ren H, Zheng Y, Ghent D, Tansey K (2021). Land surface temperature and emissivity retrieval from nighttime middle-infrared and thermal-infrared Sentinel-3 images. IEEE Geosci Remote Sens Lett, 18(5): 915–919

Parida B R, Bar S, Roberts G, Mandal S P, Pandey A C, Kumar M, Dash J (2021). Improvement in air quality and its impact on land surface temperature in major urban areas across India during the first lockdown of the pandemic. Environ Res, 199: 111280

Price J C (1983). Estimating surface temperatures from satellite thermal infrared data—a simple formulation for the atmospheric effect. Remote Sens Environ, 13(4): 353–361

Qian Y, Zhao E, Gao C, Wang N, Ma L (2015). Land surface temperature retrieval using nighttime mid-infrared channels data from airborne hyperspectral scanner. IEEE J Sel Top Appl Earth Obs Remote Sens, 8(3): 1208–1216

Qin Z, Karnieli A, Berliner P (2001). A mono-window algorithm for retrieving land surface temperature from Landsat TM data and its application to the Israel-Egypt border region. Int J Remote Sens, 22(18): 3719–3746

Quattrochi D A, Luvall J C (1999). Thermal infrared remote sensing for analysis of landscape ecological processes: methods and applications. Landsc Ecol, 14(6): 577–598

Ren H, Ye X, Nie J, Meng J, Fan W, Qin Q, Liang Y, Liu H (2022). Retrieval of land surface temperature, emissivity, and atmospheric parameters from hyperspectral thermal infrared image using a feature-band linear-format hybrid algorithm. IEEE Trans Geosci Remote Sens, 60: 1–15

Sobrino J A, Jiménez-Muñoz J C, El-Kharraz J, Gómez M, Romaguera M, Sòria G (2004). Single-channel and two-channel methods for land surface temperature retrieval from dais data and its application to the barrax site. Int J Remote Sens, 25(1): 215–230

Sobrino J A, Jiménez-Muñoz J C, Sòria G, Romaguera M, Guanter L, Moreno J, Plaza A, Martínez P (2008). Land surface emissivity retrieval from different VNIR and TIR sensors. IEEE Trans Geosci Remote Sens, 46(2): 316–327

Urban M, Eberle J, Hüttich C, Schmullius C, Herold M (2013). Comparison of satellite-derived land surface temperature and air temperature from meteorological stations on the pan-arctic scale. Remote Sens (Basel), 5(5): 2348–2367

Wan Z (2008). New refinements and validation of the MODIS Land-Surface temperature/emissivity products. Remote Sens Environ, 112(1): 59–74

Wan Z, Li Z (1997). A physics-based algorithm for retrieving land-surface emissivity and temperature from EOS/MODIS data. IEEE Trans Geosci Remote Sens, 35(4): 980–996

Wang Z, Wu X, Qian H, Yu F, Iacovazzi R, Shao X, Kondratovich V, Yoo H (2018). Radiometric Quality Assessment of GOES-16 ABI L1b Images. In: Earth Observing Systems XXIII. California: SPIE

Weng Q, Fu P, Gao F (2014). Generating daily land surface temperature at Landsat resolution by fusing Landsat and MODIS data. Remote Sens Environ, 145: 55–67

Yamamoto Y, Ishikawa H (2018). Thermal land surface emissivity for retrieving land surface temperature from Himawari-8. J Meteorol Soc Jpn, 96B(0): 43–58

Yang S, Zhang D, Sun L, Wang Y, Gao Y (2020). Assessing drought conditions in cloudy regions using reconstructed land surface temperature. J Meteorol Res, 34(2): 264–279

Ye S, Jiang W, Li J, Liu X (2017). Imaging simulation and error analysis of large field of view airborne infrared scanner. Infrared Laser Eng, 46(4): 134–139 (in Chinese)

Zarei A, Shah-Hosseini R, Ranjbar S, Hasanlou M (2021). Validation of non-linear split window algorithm for land surface temperature estimation using Sentinel-3 satellite imagery: case study; Tehran Province, Iran. Adv Space Res, 67(12): 3979–3993

Zhang R, Tian J, Su H, Sun X, Chen S, Xia J (2008). Two improvements of an operational two-layer model for terrestrial surface heat flux retrieval. Sensors (Basel), 8(10): 6165–6187

Zhu L, Zhou J, Liu S, Li M, Li G (2016). Comparison of diurnal temperature cycle model and polynomial regression technique in temporal normalization of airborne land surface temperature. In: 2016 IEEE International Geoscience and Remote Sensing Symposium (IGARSS). Beijing: IEEE: 4309–4312